THE ASTROPHYSICAL JOURNAL, 446:793–800, 1995 June 20

INFRARED CO EMISSION FROM YOUNG STARS: ACCRETION DISKS AND NEUTRAL WINDS

C. J. CHANDLER,[1] J. E. CARLSTROM,[2] AND N. Z. SCOVILLE
Owens Valley Radio Observatory 105-24, California Institute of Technology, Pasadena, CA 91125
Received 1994 August 17; accepted 1994 December 22

ABSTRACT

We have modeled the emission in the first-overtone rotation-vibration bands of CO from accretion disks and neutral winds. We compare our models with high-resolution spectra of five objects: DG Tau, SVS 13, WL 16, NGC 2024 IRS 2, and S106 IRS 4. The emission from accretion disks with accretion rates of $\sim 10^{-8}$ to $10^{-7}\ M_\odot\ \mathrm{yr}^{-1}$ successfully reproduce the fluxes, the profiles, and the optical depths of the observed spectra. We also find for several objects that the data are best reproduced by the disk model, with higher K-band extinctions to the central star than those measured by other methods. A simple wind model can also account for the flux and line profile in a number of cases, but fails to reproduce the high optical depth obtained by fitting low-resolution data. Furthermore, unreasonably high mass-loss rates are needed to reproduce the flux. However, if there are sources of heating in the wind preventing it from cooling adiabatically, the CO emission region is larger and lower mass-loss rates may be accommodated.

Subject headings: accretion, accretion disks — circumstellar matter — line: profiles — stars: mass loss — stars: pre–main-sequence

1. INTRODUCTION

The first-overtone bands of CO at 2.3 μm trace hot (3000–4000 K), dense ($n \gtrsim 10^{10}$ cm^{-3}), neutral material located within a few stellar radii of young stars. In a previous paper (Chandler et al. 1993, hereafter Paper I) we presented high-resolution spectra of the $v = 2$–0 bandhead toward five sources, SVS 13, DG Tau, WL 16, NGC 2024 IRS 2, and S106 IRS 4. Three out of the five objects display high-velocity emission (150–200 km s^{-1}) with similar bandhead profiles. DG Tau appears to have two velocity components separated by 115 km s^{-1} centered on the stellar systemic velocity, while SVS 13 displays narrow lines, with FWHM $\sim$ 50 km s^{-1}.

Given the excitation requirements and the minimum size of the CO-emitting region ($\sim$3–30 $R_\odot$; see Paper I), the only possible location for the CO-emitting material must be in a circumstellar disk or a wind. Carr (1989) presented models for disk and wind emission to match low-resolution data. Both models could account for the observed line fluxes quite well; however, the low-resolution spectra could not differentiate the two models kinematically. With the new, sensitive, high-resolution observations being carried out on the IRTF and UKIRT (Carr & Tokunaga 1992; Carr et al. 1993; Paper I), it is now possible to constrain the origin of the CO emission, and to examine the implications of the disk and wind structures in the star formation process.

This paper extends the work of Carr (1989) by modeling spectra from accretion disks and neutral winds for comparison with the new high-resolution data. We take a different approach from that of Carr et al. (1993), who fitted the emission in the $v = 2$–0 bandhead of WL 16 by isothermal gas with a power-law radial line intensity distribution, and a Keplerian rotation curve. Instead, we investigate whether the line profiles and observed intensities can be explained by the expected CO emissivity for standard disk and wind models. In § 2 we briefly describe the models, and in § 3 we compare the results with the data presented in Paper I.

2. MODELING

2.1. *Accretion disk*

The formulation for the disk is that of a steady α accretion disk (Shakura & Sunyaev 1973). It assumes that the mass accretion rate is constant throughout the disk, and that the material in the disk rotates in circular, Keplerian orbits. Angular momentum transport in the disk is achieved through the kinematic viscosity, $\nu \sim lv$, where l is the scale and v is the velocity of the largest turbulent eddies. Assuming the size scale l is less than the disk thickness H, and that the turbulence is subsonic, the kinematic viscosity is given by $\nu = \alpha c_s H$, where $\alpha \leq 1$ and c_s is the sound speed.

We follow the method described in detail by Carr (1989), so we present only the relevant equations here. The mass surface density is given by

$$\Sigma(r) = \frac{\dot{M}\mu m_{\mathrm{H}}}{6\pi\alpha kT(r)} (GM_*)^{1/2}\left[1 - \left(\frac{R_*}{r}\right)^{1/2}\right] r^{-3/2}, \qquad (1)$$

where $\dot{M}$ is the mass accretion rate in the disk, μm_{H} is the mean molecular mass (taken to be 2), $T(r)$ is the temperature in the disk as a function of radius, and M_* and R_* are the stellar mass and radius.

Assuming the disk to be isothermal perpendicular to the disk plane, the half-thickness scale height $h = H/2$ is

$$h(r) = \left[\frac{kT(r)r^3}{\mu m_{\mathrm{H}} GM_*}\right]^{1/2}, \qquad (2)$$

giving a mean density $\rho = \Sigma/2h$ of

$$\rho(r) = \frac{GM_*\dot{M}}{12\pi\alpha r^3}\left[\frac{\mu m_{\mathrm{H}}}{kT(r)}\right]^{3/2}\left[1 - \left(\frac{R_*}{r}\right)^{1/2}\right]. \qquad (3)$$

[1] Present address: National Radio Astronomy Observatory, P.O. Box O, Socorro, NM 87801. The NRAO is operated by Associated Universities, Inc., under cooperative agreement with the National Science Foundation.
[2] NSF Young Investigator.

The disk is heated both through the conversion of gravitational energy into thermal energy by the viscosity, and by the absorption of energy from the stellar radiation field. Assuming the disk to be isothermal in the z-direction, and that the disk material is in local thermodynamic equilibrium, the temperature distribution as a function of radius can be calculated by balancing the heating and cooling in the disk:

$$\frac{3GM_*\dot{M}}{8\pi r^3}\left[1-\left(\frac{R_*}{r}\right)^{1/2}\right]+\frac{\sigma T_*^4}{\pi}\left(\phi-\frac{\sin 2\phi}{2}\right)\times\left[1-e^{-\tau_c(r)/\sin\phi}\right]=\sigma T(r)^4\left[1-e^{-\tau_c(r)}\right]. \quad (4)$$

In equation (4) above, $2\phi = \sin^{-1}(R_*/r)$ is the angle subtended by the star at radius r, and $\tau_c(r)$ is the continuum optical depth measured perpendicular to the disk surface. The first term on the left-hand side of equation (4) is the viscous heating due to accretion; the second term is the heating due to the absorption of stellar radiation. The right-hand side is the cooling due to radiation. The method of solving equation (4) is discussed in detail by Carr (1989), and is not repeated here. We use the same tables of Rosseland mean opacities to calculate τ_c as Carr, from Alexander, Johnson, & Rypma (1983). Since the calculation of Rosseland mean opacities assumes that the temperature of the radiation field and the material is the same, the opacities may not be weighted appropriately for the absorbed (stellar) radiation. This problem will be more significant for the high-mass sources. To check our code, we successfully reproduced Carr's radial temperature and continuum opacity profiles, using the equations given in his paper.[3]

In fitting individual sources, the stellar mass, temperature, radius, and disk accretion rate were chosen so that the observed bolometric luminosity, L_{bol}, is the sum of the stellar luminosity, $L_* = 4\pi R_*^2\sigma T_*^4$, and the disk luminosity, $L_{disk} = GM_*\dot{M}/2R_*$. A lower limit to the inner radius of the CO-emitting region in the disk is taken to be where the temperature is 5000 K. At higher temperatures the CO is destroyed. Emission in the CO bands is seen only only where the continuum is optically thin, which was assumed to be where $\tau_c \leq 2/3$. In almost all cases the density remains above 10^{10} cm^{-3} throughout the region where CO emission arises, so we have assumed LTE when calculating the model CO level populations.

The disk was divided into rings, each of which has a characteristic double-peaked profile due to limb-brightening (cf. Smak 1981). This profile was scaled by the local Keplerian velocity and the inclination angle, i, and the contribution made by the ring to the final spectrum was calculated using the column density derived from equation (1) and the temperature obtained from solving for the heating and cooling. The profiles of individual J-lines depends on the mass of the central star, the inclination angle of the disk, and the inner and outer radii, r_i and r_o, of the CO-emitting region, all of which determine the range of Keplerian velocities observed. As the spacing between the lines decreases toward the bandhead, the double peaks of the lines can interfere constructively producing a beating pattern. The position where the beating begins is determined by the projected velocity profile. The bandhead itself can be very broad (depending on the inclination angle and the central stellar mass), with the blue and redshifted peaks separated by 200 to 300 km s^{-1}. A radial velocity offset was introduced into the model to obtain the best match with the observed spectra.

The temperature as a function of radius in the disk, for given values of M_* and R_*, depends on the accretion rate. As the accretion rate is increased keeping M_*, R_*, and L_{bol} constant, the continuum optical depth τ_c also increases, and a lower equilibrium temperature $T(r)$ is then needed to balance the heating. This result is illustrated in Figure 1 (see also Fig. 5 from Carr 1989), where we plot radial profiles of various disk properties for a model with $M_* = 1\ M_\odot$, $R_* = 5\ R_\odot$, $L_{bol} = 60\ L_\odot$, $i = 45°$, $\alpha = 1.0$, a CO abundance $X(\mathrm{CO}) = 10^{-4}$, a distance of 350 pc, and accretion rates of $1 \times 10^{-7}\ M_\odot$ yr^{-1} (*solid lines*) and $1 \times 10^{-8}\ M_\odot$ yr^{-1} (*dotted lines*). Figure 1 displays the temperature T, the continuum optical depth τ_c, the particle number density n, and the column density N, as a function of radius in the disk. The curves for $\dot{M} = 1 \times 10^{-8}\ M_\odot$ yr^{-1} demonstrate that a higher temperature is obtained at large distances compared with the higher accretion rate. We also show the velocity structure, assumed to be Keplerian. In the top panel of Figure 1 the CO flux density emitted per unit radius integrated between $\lambda = 2.292$ and 2.301 μm is displayed as a function of r. It shows that although one might expect the radial temperature decrease to result in less emission from the outer parts of the disk, this effect is approximately cancelled by the increase in emitting area. This can have important consequences for the final line profile, with slowly rotating material at large radii contributing significantly to the emission.

Two examples of synthesized spectra from the disk model with the same parameters used in Figure 1 and $\dot{M} = 1 \times 10^{-7}\ M_\odot$ yr^{-1} are displayed in Figure 2, demonstrating the beating phenomenon resulting from double-peaked velocity profiles. Figure 2*a* shows a spectrum for $i = 75°$. It has a distinctive shoulder to the blue of the nominal bandhead wavelength at λ 2.29353 μm, and the peak of the spectrum is redshifted. For this set of parameters, even the lower J-lines are beating together in the $v = 2$–0 band. Figure 2*b* shows a much more face-on disk, with $i = 15°$. The double peaks of the separate lines are quite clear, as is the position where the beating begins, at 2.297 μm.

For a typical accretion rate of $10^{-7}\ M_\odot$ yr^{-1}, with $\alpha = 1.0$ and a CO abundance of 10^{-4}, the resulting column densities imply marginally optically thick CO emission. This is in good agreement with the optical depths derived from single-temperature fits to low-resolution spectra of the bandheads toward a number of objects (Carr 1989; Thompson & Januzzi 1989; Paper I).

2.2. *Neutral Wind*

Models of neutral protostellar winds suggest that to obtain significant CO abundances, the CO molecules must be formed in the wind (e.g., Glassgold, Mamon, & Huggins 1991). Or, if the wind originates in a disk (e.g., Safier 1993), the wind must come from an inner, neutral, molecular region. Here we model both spherical and conical winds as plausible geometries for the CO-emitting region, but we also note that a disk wind may have density, temperature, and velocity distributions more similar to those in the disk model, especially close to its origin. We use the two velocity profiles assumed by Ruden, Glassgold, & Shu (1990): (i) a constant velocity wind, with $V_w = V_{max}$, and (ii) a wind which accelerates from the thermal sound speed

[3] Our eq. (1) is a factor of 3 lower than the equivalent expression in Carr (1989). A factor of 1.5 originates from an approximation used by Shakura & Sunyaev (1973), who write $d\Omega/dR \sim -\Omega/R$, where Ω is the angular velocity in the disk at radius R. Since we expect the disk to be close to Keplerian, we use the expression for Keplerian angular velocity, $d\Omega/dR = -3\Omega/2R$. A further factor of 2 comes from our prescription for the visocity. We take the largest size scale for turbulent viscosity as the full disk thickness, $H = 2h$. The formulation adopted by Carr uses $\nu = \alpha c_s h$.

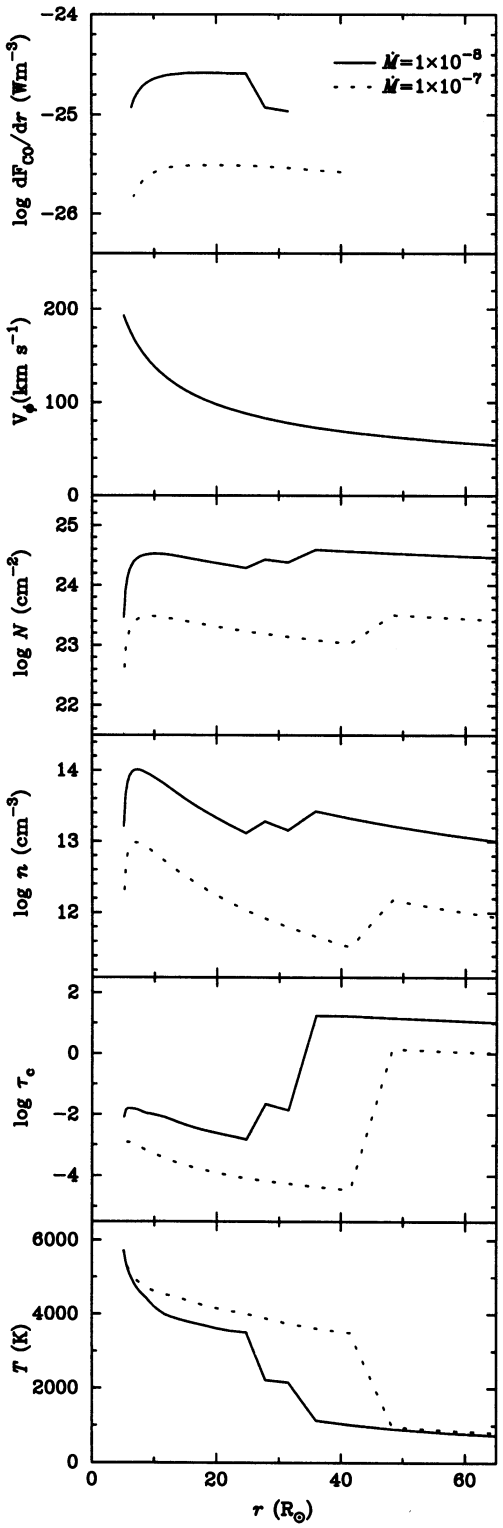

FIG. 1.—The radial distribution of various disk properties for a model with $M_* = 1\ M_\odot$, $R_* = 5\ R_\odot$, $L_{bol} = 60\ L_\odot$, $i = 45°$, $\alpha = 1.0$, $X(CO) = 10^{-4}$, $D = 350$ pc, and accretion rates of $1 \times 10^{-7}\ M_\odot\ yr^{-1}$ (*solid lines*) and $1 \times 10^{-8}\ M_\odot\ yr^{-1}$ (*dotted lines*). From top to bottom: CO flux density emitted per unit radius integrated between $\lambda = 2.292$ and 2.301 μm; azimuthal velocity; particle column density; particle number density; continuum optical depth; temperature.

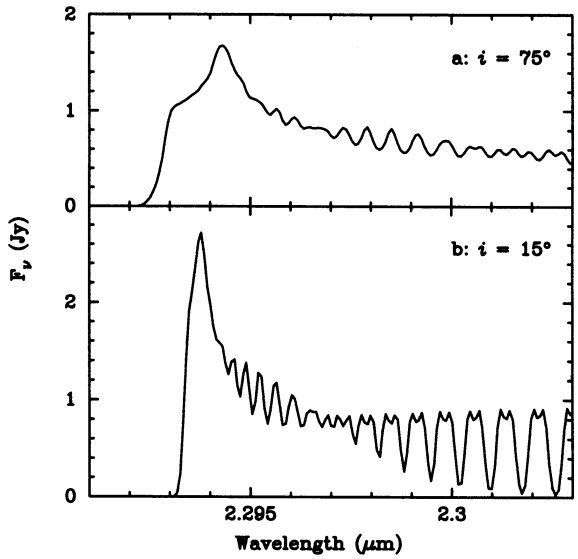

FIG. 2.—Spectra predicted by the disk model, demonstrating the phenomenon of beating resulting from double-peaked velocity profiles. (*a*) Model for $M_* = 1\ M_\odot$, $R_* = 5\ R_\odot$, $L_{bol} = 60\ L_\odot$, $i = 75°$, $\dot{M} = 1 \times 10^{-7}\ M_\odot\ yr^{-1}$, $\alpha = 1$, $X(CO) = 10^{-4}$, and a distance $D = 350$ pc. (*b*) Same as (*a*), but with $i = 15°$. In (*a*), the double-peaked profiles of the rotational lines are in phase between $\lambda = 2.297$ and 2.300 μm, and are out of phase at shorter and longer wavelengths. In (*b*), the beating occurs for $\lambda \lesssim 2.297$ μm.

close to the stellar/disk surface, approaching the terminal velocity asymptotically, with the form

$$V_w(r) = V_{max}\left(1 - \frac{R_*}{r}\right). \tag{5}$$

The terminal velocity, V_{max}, is specified in the model as a fraction of the escape velocity, so that $V_{max} = f(2GM_*/R_*)^{1/2}$. The density in the wind is determined by its semiopening angle, θ, and the mass-loss rate, $\dot{M}_w$:

$$n(r) = \frac{\dot{M}_w}{\mu m_H 4\pi r^2 (1 - \cos\theta) V_w}. \tag{6}$$

We assume $\mu = 1$ for the wind.

To calculate the temperature profile in the wind, we solve the equation for the first law of thermodynamics:

$$dU = C_V\, dT + P\, dV\,, \tag{7}$$

where $dU = \Gamma - \Lambda$ is the net energy input into the wind. For a shell at radius r, thickness Δr, optical depth $\Delta\tau = \kappa_R \rho \Delta r$ and area A, Γ is the energy absorbed from the diluted stellar radiation field:

$$\Gamma = \Omega_*\, I_*(1 - e^{-\Delta\tau})\Delta t\, A\,, \tag{8}$$

where Ω_* is the solid angle subtended by the star at radius r, $I_* = \sigma T_*^4/\pi$, and Δt can be approximated by $\Delta r/V_w$. As with the disk model, values for the Rosseland mean opacity, κ_R, are interpolated from tables in Alexander et al. (1983). It is extremely likely in the case of the wind, however, that the Rosseland mean opacity is not weighted appropriately for the absorbed stellar radiation. The energy lost due to radiation, Λ, we approximate as

$$\Lambda = 4\pi I(r)(1 - e^{-\Delta\tau})\Delta t\, A\,, \tag{9}$$

where $I(r) \approx \sigma T(r)^4/\pi$. We neglect the attenuation of the flux from the star by the intervening material in the wind, and we also neglect heating by emission from the wind itself. The net result of this simplification is an upper limit to the temperature.

The heat capacity, C_V, for the shell is

$$C_V = n\,\Delta r\,A\,\frac{3k}{2}\,. \tag{10}$$

Note that we do not include changes of state in the gas, for example, when molecules form in the wind. The work done by the material expanding from r to $r + \Delta r$ is given by

$$P\,dV = n\,\Delta r\,A\,\frac{kT}{V}\,dV\,, \tag{11}$$

where V is the volume of the shell. Writing $dV/V = 2\,\Delta r/r + dV_w/V_w$, and $dT \approx (dT/dr)\Delta r$, equations (7)–(11) give

$$[\Omega_* I_* - 4\pi I(r)](1 - e^{-\Delta\tau}) = V_w nk\,\Delta r\left(\frac{3}{2}\frac{dT}{dr} + 2\frac{T}{r} + \frac{T}{V_w}\frac{dV_w}{dr}\right). \tag{12}$$

We solve equation (12) iteratively.

Figure 3 compares the temperature T derived by the above method as a function of radius with the temperature profile obtained by Ruden et al. (1990) for the same wind parameters. Our model profiles are plotted as solid lines and are denoted C1 and C2. The equivalent profiles from the Ruden et al. models are denoted S1 and S2 and are plotted as dotted lines. The gas and dust temperatures are calculated explicitly by Ruden et al., while our formulation assumes the gas and dust to be sufficiently coupled that the temperatures are the same. All models assume a spherical wind ($\theta = 90°$), a mass-loss rate $\dot{M}_w$ of $3 \times 10^{-6}\,M_\odot\ \mathrm{yr}^{-1}$, and $V_{\max} = 150\ \mathrm{km\ s}^{-1}$. Models S1 and C1 are for a constant velocity wind, and S2 and C2 are for an accelerated wind, with the velocity distribution described by equation (5). We also plot the velocity and density profiles (eqs. [5] and [6]) for comparison with the temperature distribution. The stellar temperature and radius are 5000 K and 9.5 $R_\odot$, respectively, giving $L_* = 50\,L_\odot$.

The differences between the temperature distributions in models C1 and C2 for $r/R_* < 3$ are due to the significantly different density profiles resulting from the velocity laws assumed. Model C2, where the wind accelerates from the sound speed at the stellar surface and approaches $V_{\max}$ asymptotically, has considerably higher densities close to the star compared with C1. The higher densities correspond to higher opacities and allow the wind in model C2 to cool more quickly than in C1. At large radii, where the velocities in both models are similar, the temperature profiles converge. Our use of the Rosseland mean opacities assumes that the abundances of molecular, atomic, and ionic species in the wind are those of a cool star. The more detailed calculation performed by Ruden et al. (1990) does not make this assumption. It includes the heating due to chemical reactions, ambipolar diffusion, and the formation of silicate grains explicitly, but does not include the opacity due to atomic and molecular line transitions which accounts for our bump at $\sim$2000 K in models C1 and C2.

In calculating the CO emission from the wind we assume that no CO exists where the temperature is higher than 5000 K, defining the inner radius for the emission region. The outer radius is determined by when the density falls below $10^{10}\ \mathrm{cm}^{-3}$ (this occurs at $r/R_* \gtrsim 12$ for models shown in Fig. 3), although once the temperature drops below $\sim$1000 K there is no significant contribution to the total emission because in LTE the population of the $v = 2$ level is too low.

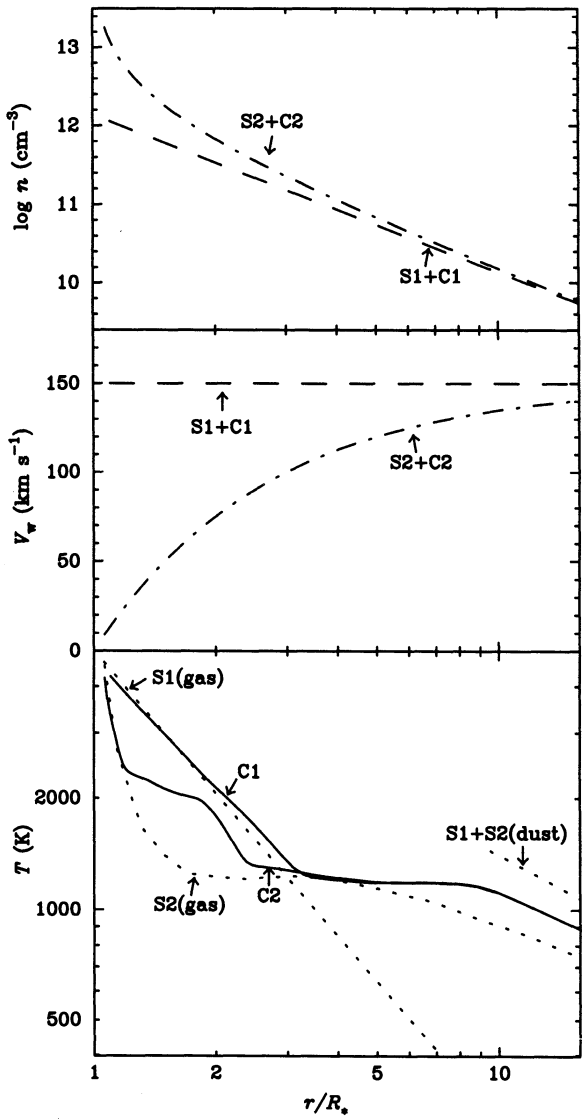

FIG. 3.—Temperature as a function of radius for various wind models. The solid lines, C1 and C2, are temperature profiles derived using the method described in the text. The dotted lines, S1 and S2, are the temperature profiles for the gas and dust (plotted separately) obtained by Ruden et al. (1990) for the same wind parameters. The models have $R_* = 9.5\ R_\odot$, $L_* = 50\ L_\odot$, $V_{\max} = 150\ \mathrm{km\ s}^{-1}$, $\dot{M}_w = 3 \times 10^{-6}\,M_\odot\ \mathrm{yr}^{-1}$, and $\theta = 90°$. Models S1 and C1 have a constant velocity wind, and S2 and C2 have velocity profiles described by eq. (5). The velocity and density profiles described by eqs. (5) and (6) are also shown.

There will be other sources of heating in the wind besides the stellar radiation field, for example, the acceleration mechanism. To account for the most extreme case, we also produce model spectra for a wind where the temperature is maintained at a constant temperature.

The numerical method is very similar to the disk model. The velocity profile of a shell of constant radius was calculated for a given θ, and inclination angle, i, of the cone. The sphere or cone was divided into shells, and the profile was scaled by the local wind velocity from equation (5). The contribution made by the shell was then calculated for the relevant density and temperature.

The profiles of the individual J-lines depend sensitively on both the temperature and velocity distributions in the wind. For high-mass sources, the relevant temperature for CO emission occurs at large distances from the star, and there is little distinction between the accelerated and constant velocity winds. For the low-mass objects the temperature drops very quickly due to adiabatic cooling, and the CO emission originates very close to the star. The precise form of the velocity distribution is therefore important. For the velocity distribution of the accelerated wind described by equation (5), the material close to the star is moving slowly, and narrow, single-peaked lines will result for all orientations and cone opening angles. If a high temperature can be maintained at some distance from the star by an unspecified heating mechanism (which we approximate here by a constant temperature wind), the velocity of the CO-emitting material can be quite high, and the line profiles then depend on the semiopening angle θ, and the inclination angle i. For the constant velocity wind even the adiabatically cooling temperature distribution may give broad line profiles.

When the CO emission originates from high-velocity material, the profiles of the individual J-lines may be distinctly double-peaked, just broad, or quite narrow if the wind is conical and in the plane of the sky. If there is no component of the wind in the plane of the sky, so that $\theta < 90° - i$, the line profiles are double peaked, with separated blue and redshifted components (Fig. 4*a*). These line profiles are different from those obtained for the disk model, however, in the essential feature that there is little emission from material at $V = 0$ km s^{-1}. While the disk profiles are also double-peaked, there is always continuous emission connecting the blue and red components.

When part of the wind lies in the plane of the sky, so that $\theta > 90° - i$, the velocity profile is single-peaked. If $\theta \approx 90° - i$, the profile is double-peaked, with significant emission at $V = 0$ also. Under these circumstances, the observed profiles can be similar to the disk model. The width of the lines in the wind model is determined by the wind acceleration law, the inclination angle, and the opening angle of the cone. In the extreme case of a spherical wind, where the velocity profile is flat-topped, the resulting bandhead profile is single-peaked and very broad. The spectrum for a spherical wind is shown in Figure 4*b*. For reasonable mass-loss rates of $\sim 10^{-7}\ M_\odot$ yr^{-1}, the CO emission in the wind model is predicted to be optically thin.

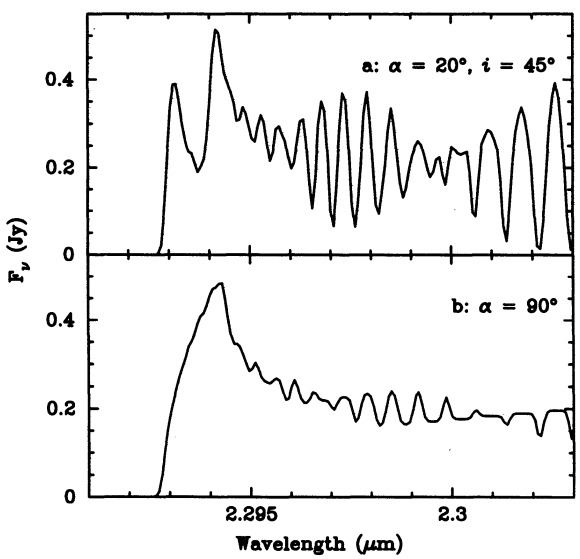

FIG. 4.—Spectra predicted by the accelerated wind model, with V_w described by eq. (5). (*a*) Model for $M_* = 1\ M_\odot$, $R_* = 3\ R_\odot$, $L_{bol} = 10\ L_\odot$, $V_{max} = 100$ km s^{-1}, $D = 140$ pc, $\dot{M}_w = 1 \times 10^{-6}\ M_\odot$ yr^{-1}, $\theta = 20°$, and $i = 45°$. Note the well-separated blue and redshifted components of the bandhead. (*b*) Same as (*a*), but with $\theta = 90°$ (i.e., a spherically symmetric wind).

3. RESULTS FOR INDIVIDUAL SOURCES

3.1. *DG Tau*

We find good agreement between DG Tau and our model spectra of a collimated, conical wind. The model presented in Figure 5 is for an adiabatically cooling wind, and a velocity profile described by equation (5), with $f = 0.3$. The semiopening angle is $\theta = 25°$, the inclination angle is $i = 55°$, and the mass-loss rate is $8 \times 10^{-7}\ M_\odot$ yr^{-1}. The stellar parameters (mass, radius, luminosity, etc.) assumed for DG Tau are listed in Table 1. An adjustment to the radial velocity of ~ 7 km s^{-1} (approximately half a resolution element) has been applied to the model in Figure 5, well within the uncertainties of the wavelength calibration.

The above mass-loss rate is a factor of 20 higher than that derived from the radio continuum emission, and a factor of 300 higher than the optical jet (Mundt, Brugel, & Bührke 1987). However, the mass-loss rate in the model needed to match the observed flux in the DG Tau bandhead can be lowered by a factor of 10 if the temperature in the wind can be maintained at 2850 K (chosen to match the low-resolution data: Paper I) out to where the density falls below 10^{10} cm^{-3} ($\sim 70\ R_\odot$ for the above values of θ, $\dot{M}_w$, and V_{max}).

It is interesting to note that both red and blueshifted emission is seen from DG Tau in optical emission lines (sodium, Hα), suggesting that there is no optically thick obscuring material (such as a disk) very close to the star. The photospheric features are, however, heavily veiled (Hartigan et al. 1990), implying that perhaps the veiling is due to chromospheric emission rather than a boundary layer in this source.

We find that our disk models cannot reproduce the profile of the bandheads in the spectrum of DG Tau without including the contamination of stellar photospheric features, which is highly likely for this source (Paper I).

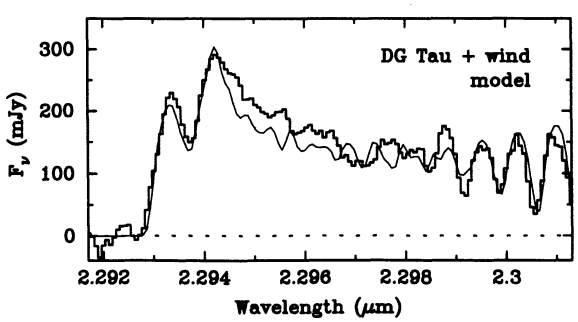

FIG. 5.—The CO $v = 2$–0 bandhead of DG Tau (histogram), together with the best-fit model spectrum of a neutral wind. The stellar properties assumed for DG Tau are listed in Table 1. The other parameters used in the wind model are $i = 55°$, $\theta = 25°$, $\dot{M}_w = 8 \times 10^{-7}\ M_\odot$ yr^{-1}, and $f = 0.3$ ($V_{max} = 110$ km s^{-1} in eq. [5]). The temperature distribution is calculated assuming adiabatic cooling.

TABLE 1

STELLAR PROPERTIES ASSUMED IN OUR DISK AND WIND MODELS

Source	M_* ($M_\odot$)	R_* ($R_\odot$)	L_{bol} ($L_\odot$)	D (pc)	A_K (mag)
DG Tau	1	3	9.6	140	0.24
SVS 13	1	5	66	350	1.0
WL 16	2.5	3	22	160	2.3
NGC 2024 IRS 2	15	6	1×10^4	415	2.05
S106 IRS 4	25	8	8×10^4	1200	1.35

3.2. *SVS 13*

To fit both the shape and the flux of SVS 13 with a Keplerian disk, we require an inclination angle of only 12° (i.e., almost face-on), an accretion rate of 5×10^{-7} $M_\odot$ yr^{-1}, and an extinction of 3.5 magnitudes at K (Fig. 6). This extinction is similar to that reported by Carr (1989). A radial velocity of 9 km s^{-1} has been used in the model.

The small inclination angle is needed to fit the beating of the high J-lines close to the bandhead, while maintaining single-peaked lines (to within our resolution) away from the bandhead. However, the lower J-lines are then slightly too narrow, and there is a small excess to the blue of the bandhead itself. Although the inclination angle of the HH objects is somewhat larger, we argue in Paper I that a face-on disk is not unreasonable for SVS 13.

If the emission from SVS 13 does arise from a face-on disk, we may then need a mechanism to broaden the lines to 40–50 km s^{-1} (Carr & Tokunaga 1992; Paper I). One possibility is that the CO emission region is located at the base of a disk wind, where material begins to be accelerated away from the disk surface. Another possibility is that the disk in SVS 13 is rotating at speeds slower than Keplerian. If the inner regions of the disk were, for example, forced to corotate with the central star by a strong magnetic field threading the disk (Najita et al. 1994), the emission lines would be narrower at intermediate inclination angles.

The emission from a wind faces similar problems to a disk. We know the wind to have velocities of $\sim$200 km s^{-1} close to the star from the width of the Brγ line (Carr & Tokunaga 1992). The predicted width of the CO emission lines from such a wind would be much too broad unless the wind were confined to a cone in the plane of the sky outside the Brγ emission zone. Again, this orientation is inconsistent with the large-scale outflow, and with the high radial velocities seen in the HH objects and in pure rotational lines of CO (cf. Bachiller & Cernicharo 1990).

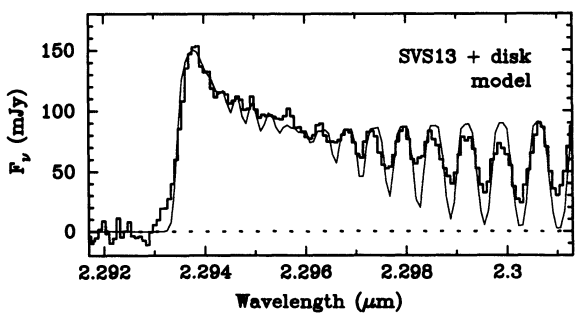

FIG. 6.—The CO $v = 2$–0 bandhead of SVS 13 (*histogram*), together with the best-fit model spectrum of an accretion disk. The parameters used in the disk model are $i = 12°$, $\dot{M} = 5 \times 10^{-7}$ $M_\odot$ yr^{-1}, $\alpha = 1$, $X(\mathrm{CO}) = 10^{-4}$, and $A_K = 3.5$.

3.3. *WL 16*

Constraints have been placed on the properties of the central star of WL 16 by Carr et al. (1993), assuming the CO bandhead emission arises in a disk. We find that in order to reproduce the high velocities seen in its spectrum with our disk model, we need to use the upper limit to the stellar mass obtained from their work of 2.5 $M_\odot$. A range of parameters fit the spectrum equally well, for $R_* = 2$–4 $R_\odot$, $\dot{M} = 2$–3 $\times 10^{-8}$ $M_\odot$ yr^{-1}, $A_K = 2.0$–2.5, and $i = 65°$–80°. The model displayed in Figure 7*a* has $R_* = 3$ $R_\odot$, $\dot{M} = 2.5 \times 10^{-8}$ $M_\odot$ yr^{-1}, $A_K = 2.3$, and $i = 70°$, and a radial velocity of 30 km s^{-1}. The CO emission originates from 4.2 to 18 $R_\odot$, where the material has a temperature in the range 4000–5000 K. The relatively low accretion rate in the model results in a rather limited range of temperatures where the CO emission originates (cf. Fig. 1), and explains why the isothermal model used by Carr et al. (1993) looks similar to our best fit.

WL 16 is an unusual source; while its infrared spectral energy distribution is characteristic of a deeply embedded young star (Adams, Lada, & Shu 1987), its circumstellar material remains undetected at $\lambda = 1.3$ mm down to 3 σ limits of 7 mJy (André et al. 1990). However, the *IRAS* data suffer from confusion in the Ophiuchus region, and it may be that it is actually more evolved than suggested by the infrared data. If this is the case, the low accretion rate implied by our CO model compared with SVS 13 may be indicative of its later stage of evolution.

The wind model with adiabatic cooling cannot fit the profile of WL 16. There is too much emission from cold material, which produces fluxes which are too high in the low J-lines away from the bandhead. If the temperature of the wind can be

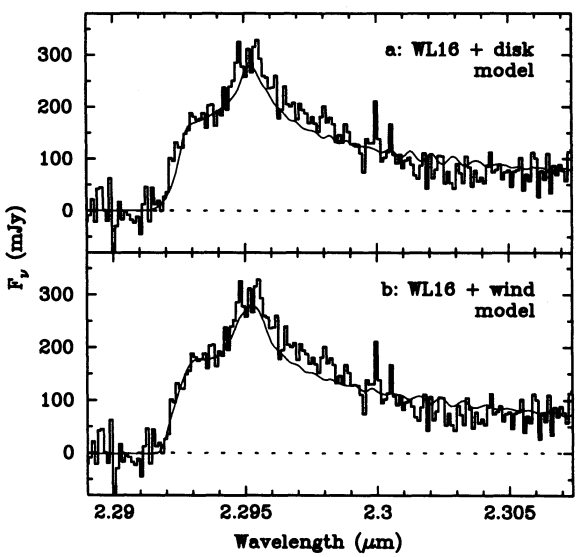

FIG. 7.—(*a*) The CO $v = 2$–0 bandhead of WL 16, with the disk model. A range of parameters fit the shape of the spectrum; the model shown has $i = 70°$, $\dot{M} = 2.5 \times 10^{-8}$ $M_\odot$ yr^{-1}, $\alpha = 1$, $X(\mathrm{CO}) = 10^{-4}$, and $A_K = 2.3$. (*b*) The spectrum of WL 16, with the wind model. As with the disk, a wide range of parameters fit the bandhead; the model shown has $\theta = 70°$, $i = 20°$, $\dot{M}_w = 9 \times 10^{-7}$ $M_\odot$ yr^{-1}, and $f = 0.7$ with a constant velocity wind ($V_w = 390$ km s^{-1}). The temperature of the wind is constant at 4000 K, out to where the density falls below 10^{10} cm^{-3} at $r = 150$ $R_\odot$.

maintained at 4000 K, which is needed to match the low-resolution data of Geballe & Persson (1987), the bandhead can be fitted by a wide range of model parameters, with mass-loss rates of 6×10^{-7} to $1 \times 10^{-6}\ M_\odot\ \mathrm{yr}^{-1}$ for values of A_K in the range 2.0–2.5. Both constant velocity and accelerating winds fit equally well, if $f \gtrsim 0.5$. Combinations of $i + \theta \approx 90°$ are needed to fit the shape of the bandhead. The model in Figure 7*b* is for the constant temperature, constant velocity wind, with $f = 0.7$, $\theta = 20°$, $i = 70°$, and $\dot{M}_w = 9 \times 10^{-7}\ M_\odot\ \mathrm{yr}^{-1}$.

3.4. *NGC 2024 IRS 2*

It is difficult to fit the spectrum of NGC 2024 with the disk model using the measured extinction of $A_V = 20.5$ (Maihara, Mizutani, & Suto 1990), equivalent to $A_K = 2$. The accretion rates needed to reproduce the CO bandhead fluxes are too low to make the emission optically thick, as observed. For a CO abundance of 10^{-4}, we find acceptable fits if we use $A_K = 4.4$. The model in Figure 8*a* uses the stellar parameters in Table 1, $i = 33°$, $\dot{M} = 5 \times 10^{-7}\ M_\odot\ \mathrm{yr}^{-1}$, and a radial velocity of 0 km s^{-1}. It is not unreasonable to expect the extinction to be higher toward the central star and disk than that derived toward the Brγ and Brα-emitting region (Maihara et al. 1990). The model does not do well at reproducing details in the spectrum away from the bandhead, but spectra with greater wavelength coverage are needed to determine the severity of this problem. The emission in the disk model arises at radii of 60–180 $R_\odot$, where the Keplerian velocities are 130–220 km s^{-1}. It is quite likely that the material in the disk will not be smoothly distributed as in equation (1), and instead may be clumpy due to instabilities in the disk. This may account for the detailed differences between the data and the disk model.

The wind model with adiabatic cooling requires mass-loss rates in the range 5×10^{-6} to $3 \times 10^{-5}\ M_\odot\ \mathrm{yr}^{-1}$. Acceptable fits were found for constant velocity winds and accelerating winds, with $0.1 \lesssim f \lesssim 0.5$ ($100 \lesssim V_{\max} \lesssim 500$ km s^{-1}), and $\theta + i \approx 90°$. Figure 8*b* shows a model for $f = 0.3$, a velocity profile described by equation (5), $\theta = 13°$, $i = 78°$, and $\dot{M}_w = 1.5 \times 10^{-5}\ M_\odot\ \mathrm{yr}^{-1}$. The stellar heating is extremely important for the high-mass objects, and results in material with temperatures of $\sim$2000 K out to an AU or more. The outer radius of the CO-emitting region at these radii is determined by where the density falls below 10^{10} cm^{-3}, so the constant-temperature wind model gives similar results to the adiabatically cooling wind. The wind model predicts the emission to be optically thin, with a significant contribution from cooler material $T \lesssim 3000$ K, to account for the flux in the low J-lines compared with the bandhead.

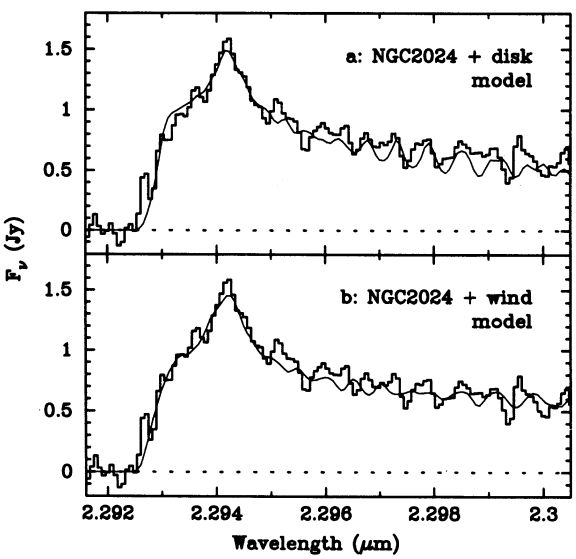

FIG. 8.—(*a*) The CO $v = 2$–0 bandhead of NGC 2024 IRS 2, with the disk model. The parameters of this fit are $i = 33°$, $\dot{M} = 5 \times 10^{-7}\ M_\odot\ \mathrm{yr}^{-1}$, $\alpha = 1$, $X(\mathrm{CO}) = 10^{-4}$, and $A_K = 4.4$. (*b*) Same as (*a*), with the wind model. The stellar properties assumed are listed in Table 1. The other parameters are $\theta = 13°$, $i = 78°$, $\dot{M}_w = 1.5 \times 10^{-5}\ M_\odot\ \mathrm{yr}^{-1}$, and $f = 0.3$ ($V_{\max} = 290$ km s^{-1} in eq. [5]). The temperature distribution is calculated allowing adiabatic cooling.

3.5. *S106 IRS 4*

We find the worst fit is for our lowest quality spectrum, S106. To prevent too much cold material from contributing to the emission from the low J-lines away from the bandhead in the high-resolution spectrum, and to reproduce the high excitation temperature of 4800 K seen in low-resolution data (Paper I), we had to impose an artificial outer cutoff radius. Furthermore, the data show a sharp edge to the blueshifted emission at the bandhead, and a narrow peak at the redshifted component, which require a narrow ring of emission in order to be reproduced by the disk model. The model shown for S106 in Figure 9 has an outer cutoff radius, with the CO emission arising from $175 \lesssim r \lesssim 320\ R_\odot$, $i = 65°$, $\dot{M} = 5 \times 10^{-7}\ M_\odot\ \mathrm{yr}^{-1}$, $A_K = 4.0$, and a radial velocity of -30 km s^{-1}. As with NGC 2024, we need a higher extinction than that generally measured for the S106 cluster. We can accommodate lower values of A_K by decreasing the outer cutoff radius. Note that we use the newly determined distance to S106 of 1.2 kpc (Rayner 1994).

The wind model has extreme difficulty in reproducing the sharpness of the bandhead in S106 without also having distinct red and blueshifted components. As with NGC 2024, stellar heating pushes the relevant temperatures for CO emission out to $\sim$1 AU from the star. Our failure to fit the spectrum of S106 with the wind model does not rule out a wind as the origin of some of the CO emission, but emission from another location (for example, a disk) is also needed.

4. CONCLUSIONS

We have modeled the CO $v = 2$–0 bandhead emission from accretion disks and neutral winds around young stars, to investigate whether they can account for the spectra presented in Paper I. Accretion disks are able to reproduce the observed fluxes, the line profiles, and optical depths for all the sources

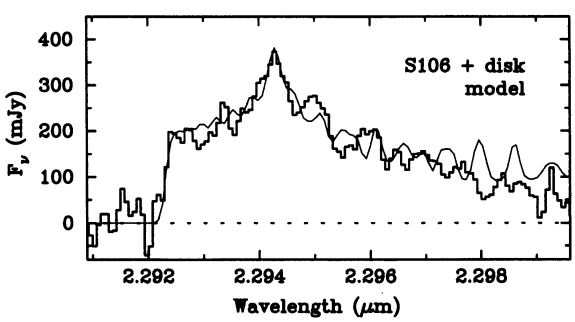

FIG. 9.—The CO $v = 2$–0 bandhead of S106 IRS 4 (*histogram*), together with the best-fit model spectrum of an accretion disk. The parameters used in this model are $i = 65°$, $\dot{M} = 5 \times 10^{-7}\ M_\odot\ \mathrm{yr}^{-1}$, $\alpha = 1$, $X(\mathrm{CO}) = 10^{-4}$, and $A_K = 4.0$. This model also includes an outer cutoff radius to the CO-emitting region, to reproduce the sharp edge at the bandhead.

apart from DG Tau. In the case of DG Tau, the observed profile cannot be explained by a disk without the inclusion of contamination of the spectrum by stellar photospheric absorption features (Paper I). Accretion rates of $\sim 5 \times 10^{-7} M_{\odot}$ yr^{-1} are found for SVS 13, NGC 2024, and S106. WL 16 is well modeled by a disk, but with an accretion rate an order of magnitude lower than the other sources. We suggest this may be indicative of its later stage of evolution compared with the embedded source SVS 13. For a number of objects, we find the best fit to the observed spectra using higher K-band extinctions than those measured by other methods, or extrapolated from the optical. This probably indicates that those other measurements are not penetrating as far as the central disk/star, either because the extinction is too high, or the diagnostic used is not tracing the same material that we see.

A simple wind model allowed to cool adiabatically is able to reproduce the observed flux and the line profile for DG Tau and NGC 2024. However, the DG Tau profile is likely to be contaminated by underlying photospheric absorption features (Paper I). The wind model can also reproduce the flux and line profile of WL 16, provided the temperature in the wind can be maintained at $\sim$4000 K. However, the emission from a wind is predicted to be optically thin, which is not in agreement with many low-resolution measurements (Thompson & Januzzi 1989; Paper I). Furthermore, exceptionally high mass-loss rates are needed to reproduce the flux. We feel it is unlikely that the emission in SVS 13 and S106 arises purely from a wind; however, a combination of disk and wind is viable.

Since the disk model reproduces more of the observed features of the CO $v = 2$–0 bandhead spectra, we prefer the disk as the origin of the emission. In order to constrain the models further, and to test their predictability, high-resolution observations of the lower J-lines in the $v = 2$–0 band, and of the first overtone bands from higher vibrational levels, will be most useful.

We thank the referee for useful comments which helped improve this paper. C. J. C. was funded by a SERC/NATO Fellowship during part of this work. The Owens Valley Radio Observatory is funded by NSF grant AST 93-14079.

REFERENCES

Adams, F. C., Lada, C. J., & Shu, F. H. 1987, ApJ, 312, 788
Alexander, D. R., Johnson, H. R., & Rypma, R. L. 1983, ApJ, 272, 773
André, P., Montmerle, T., Feigelson, E. D., & Steppe, H. 1990, A&A, 240, 321
Bachiller, R., & Cernicharo, J. 1990, A&A, 239, 276
Carr, J. S. 1989, ApJ, 345, 522
Carr, J. S., & Tokunaga, A. T. 1992, ApJ, 393, L67
Carr, J. S., Tokunaga, A. T., Najita, J., Shu, F. H., & Glassgold, A. E. 1993, ApJ, 411, L37
Chandler, C. J., Carlstrom, J. E., Scoville, N. Z., Dent, W. R. F., & Geballe, T. R. 1993, ApJ, 412, L71 (Paper I)
Geballe, T. R., & Persson, S. E. 1987, ApJ, 312, 297
Glassgold, A. E., Mamon, G. A., & Huggins, P. J. 1991, ApJ, 373, 254
Hartigan, P., Hartmann, L., Kenyon, S. J., Strom, S. E., & Skrutskie, M. F. 1990, ApJ, 354, L25
Maihara, T., Mizutani, K., & Suto, H. 1990, ApJ, 354, 549
Mundt, R., Brugel, E. W., & Bührke, T. 1987, ApJ, 319, 275
Najita, J., Ostriker, E., Wilkin, F., Johns, C. M., & Carr, J. 1994, in Clouds, Cores, and Low Mass Stars, ed. D. P. Clemens & R. Barvainis (ASP Conf. Ser., 65), 325
Rayner, J. 1994, in Infrared Astronomy with Arrays: The Next Generation, ed. I. S. McLean (Dordrecht: Kluwer), 185
Ruden, S. P., Glassgold, A. E., & Shu, F. H. 1990, ApJ, 361, 546
Safier, P. N. 1993, ApJ, 408, 115
Shakura, N. I., & Sunyaev, R. A. 1973, A&A, 24, 337
Smak, J. 1981, Acta Astron., 31, 395
Thompson, R. I., & Januzzi, B. T. 1989, 344, 799